

# A non-contact wearable device for monitoring epidermal molecular flux

<https://doi.org/10.1038/s41586-025-08825-2>

Received: 13 May 2024

Accepted: 21 February 2025

Published online: 9 April 2025

 Check for updates

Jaeho Shin<sup>1,2,24</sup>, Joseph Woojin Song<sup>1,3,4,5,24</sup>, Matthew Thomas Flavin<sup>1,6,24</sup>, Seunghee Cho<sup>1,24</sup>, Shupeng Li<sup>2,24</sup>, Ansen Tan<sup>1,3,4</sup>, Kyung Rok Pyun<sup>1</sup>, Aaron G Huang<sup>1,8</sup>, Hui Feng Wang<sup>3,4</sup>, Seongmin Jeong<sup>2</sup>, Kenneth E. Madsen<sup>1,9</sup>, Jacob Trueb<sup>1</sup>, Mirae Kim<sup>3,4</sup>, Katelynn Nguyen<sup>1</sup>, Angela Yang<sup>10</sup>, Yaching Hsu<sup>8</sup>, Winnie Sung<sup>1</sup>, Jiwon Lee<sup>11,12</sup>, Sooyeon Phyoo<sup>11,13</sup>, Ji-Hoon Kim<sup>2,14</sup>, Anthony Banks<sup>1,8</sup>, Jan-Kai Chang<sup>1,8</sup>, Amy S. Paller<sup>10</sup>, Yonggang Huang<sup>1,7,15</sup>, Guillermo A. Ameer<sup>1,3,4,16,17</sup> & John A. Rogers<sup>1,3,4,8,10,18,19,20,21,22,23</sup>

Existing wearable technologies rely on physical coupling to the body to establish optical<sup>1,2</sup>, fluidic<sup>3,4</sup>, thermal<sup>5,6</sup> and/or mechanical<sup>7,8</sup> measurement interfaces. Here we present a class of wearable device platforms that instead relies on physical decoupling to define an enclosed chamber immediately adjacent to the skin surface. Streams of vapourized molecular substances that pass out of or into the skin alter the properties of the microclimate defined in this chamber in ways that can be precisely quantified using an integrated collection of wireless sensors. A programmable, bistable valve dynamically controls access to the surrounding environment, thereby creating a transient response that can be quantitatively related to the inward and outward fluxes of the targeted species by analysing the time-dependent readings from the sensors. The systems reported here offer unique capabilities in measuring the flux of water vapour, volatile organic compounds and carbon dioxide from various locations on the body, each with distinct relevance to clinical care and/or exposure to hazardous vapours. Studies of healing processes associated with dermal wounds in models of healthy and diabetic mice and of responses in models using infected wounds reveal characteristic flux variations that provide important insights, particularly in scenarios in which the non-contact operation of the devices avoids potential damage to fragile tissues.

The skin forms our primary interface with the environment, and the movement of chemical species into and out of the skin surface can substantially influence health. These fluxes include water, an abundant species in the body and the atmosphere, as well as volatile organic compounds (VOCs), carbon dioxide ( $\text{CO}_2$ ) and other medically important compounds<sup>9–12</sup>. Imbalanced outward water-vapour fluxes often indicate dysfunction in cutaneous homeostasis<sup>9</sup>, whereas certain pathologies and infections at wound sites can be linked to the emissions of vapourized chemicals<sup>10,11</sup>. Inward fluxes of substances provide valuable insights into the effects of atmospheric chemicals on health<sup>13</sup>. Existing wearable devices use microfluidic networks for precise monitoring of the time-dependent flow of liquids, such as sweat<sup>14,15</sup>, from the surface of the skin; but these and other approaches do not apply to gases. We present

a compact, wireless platform designed for continuous, quantitative monitoring of gaseous fluxes into and out of the skin at sequential time points through repeated cycles of transient measurements. The capabilities of the platform derive from the time-dependent modulation between open and closed modes of a defined microclimate immediately adjacent to the skin, in contrast to existing static systems<sup>16–19</sup>. The non-contact proximity operation principle contrasts with that of conventional wearable devices that require direct physical contact with the body. This technology can provide unique insights for clinical decision-makers managing conditions such as dermatological diseases and dermal wounds, as well as an improved understanding of underlying pathophysiologies. Moreover, the device enables the monitoring of hazardous atmospheric chemicals that enter the body through the

<sup>1</sup>Querry-Simpson Institute for Bioelectronics, Northwestern University, Evanston, IL, USA. <sup>2</sup>Center for Advanced Molecular Recognition, Korea Institute of Science and Technology, Seoul, South Korea. <sup>3</sup>Department of Biomedical Engineering, Northwestern University, Evanston, IL, USA. <sup>4</sup>Center for Advanced Regenerative Engineering, Northwestern University, Evanston, IL, USA. <sup>5</sup>Chan Zuckerberg Biohub Chicago, Chicago, IL, USA. <sup>6</sup>School of Electrical and Computer Engineering, Georgia Institute of Technology, Atlanta, GA, USA. <sup>7</sup>Department of Mechanical Engineering, Northwestern University, Evanston, IL, USA. <sup>8</sup>Wearifi Inc, Northfield, IL, USA. <sup>9</sup>Department of Chemistry, University of Illinois at Urbana-Champaign, Urbana, IL, USA. <sup>10</sup>Department of Dermatology, Northwestern University Feinberg School of Medicine, Chicago, IL, USA. <sup>11</sup>Center for Climate and Carbon Cycle Research, Korea Institute of Science and Technology, Seoul, South Korea. <sup>12</sup>Division of Energy and Environment Technology, Korea Institute of Science and Technology, Seoul, South Korea. <sup>13</sup>Department of Materials Science and Engineering, Korea University, Seoul, South Korea. <sup>14</sup>Department of KHU-KIST Convergence Science and Technology, Kyung Hee University, Seoul, South Korea. <sup>15</sup>Department of Civil Engineering, Northwestern University, Evanston, IL, USA. <sup>16</sup>Department of Materials Science and Engineering, Northwestern University, Evanston, IL, USA. <sup>17</sup>International Institute for Nanotechnology, Northwestern University, Evanston, IL, USA. <sup>18</sup>Department of Materials Science and Engineering, Northwestern University, Evanston, IL, USA. <sup>19</sup>Department of Dermatology, Northwestern University, Evanston, IL, USA. <sup>20</sup>Department of Neurological Surgery, Northwestern University, Evanston, IL, USA. <sup>21</sup>Department of Chemical Engineering, Northwestern University, Evanston, IL, USA. <sup>22</sup>Department of Electrical Engineering and Computer Science, Northwestern University, Evanston, IL, USA. <sup>23</sup>These authors contributed equally: Jaeho Shin, Joseph Woojin Song, Matthew Thomas Flavin, Seunghee Cho, Shupeng Li. <sup>24</sup>e-mail: y-huang@northwestern.edu; g-ameer@northwestern.edu; jrogers@northwestern.edu

skin. We describe these applications along with the engineering and physics behind the system, enabling quantitative analysis of the skin flux and related intrinsic parameters from the measured data.

## Design and operating principles

Demonstrations of this epidermal flux sensor (EFS; Fig. 1a) focus on water vapour, VOCs and CO<sub>2</sub>—important indicators of skin barrier function<sup>9</sup>, body homeostasis<sup>20,21</sup>, environmental safety<sup>13</sup> and wound healing<sup>22,23</sup>. The device, a compact module, can be coupled to various skin locations (Fig. 1b). It features three main subsystems: (1) a chamber with sensors to measure concentrations of targeted species in the chamber ( $c_c$ ) and skin properties; (2) a programmable valve to modulate chamber ventilation, thereby influencing  $c_c$ ; and (3) an electronic circuit for operation, data acquisition and wireless communication with a user interface (a smartphone). Sensors suspended in the chamber capture dynamic changes in  $c_c$  before and after valve actuation. Additional sensors at the base of the chamber measure the temperature, electrical impedance and thermal conductivity of the skin, providing contextual information. Weighing only 11 g, the EFS operates for at least one day without requiring a recharge. Figure 1c illustrates the overall device structure. Supplementary Note 1 provides further details on the third subsystem and hardware components.

A thin electromagnetic coil in the valve actuates a permanent magnetic disc to switch the chamber between open and closed states across a bistable magnetic potential created by soft magnets (Fig. 1d). When open, basal flux passes in or out depending on the concentration gradient across the skin and the ambient air. Rapid valve closing (<10 ms) yields dynamic changes in  $c_c$ , dictated by the flux into or out of the skin. Figure 1e shows the time-dependent  $c_c$  values of water vapour due to transepidermal water loss (TEWL) and ethanol vapour due to inward diffusion from a concentrated ambient environment. Cyclic valve actuation renders opposite variations in  $c_c$ , corresponding to the outflux and influx of these gases. The initial change in  $c_c$  immediately after valve closure ( $\partial c_c / \partial t|_{t=0}$ ) reflects the natural flux density,  $f$  (Fig. 1f). To precisely calculate  $f$ , spatiotemporal non-uniformities in the microclimate and the occlusive effect of the EFS must be compensated for.

The compensation scheme and quantitative analyses rely on a computational model. Figure 1f (bottom) displays simulations of the flux-density profiles in the microclimate during the first few seconds after valve closure. The findings establish an empirical relationship that is valid across practical ranges (equation (1)):

$$\tilde{f} = k(V/S \times \partial c_c / \partial t|_{t=0}) \quad (1)$$

where  $\tilde{f}$  is the flux density before valve closure,  $k$  is the correction coefficient,  $V$  is the chamber volume and  $S$  is the skin area. Simulations indicate that the  $k$  for water vapour is 0.92. Supplementary Note 2 provides the measurement, design and operating principles. Measurements rely on stable skin–chamber coupling, maintained through the engineering solutions described in Supplementary Note 3.

## Epidermal flux of water

The epidermal flux of water vapour represents a crucial aspect of overall homeostasis<sup>20,21</sup>. This flux ( $f_w$ ) includes contributions from TEWL ( $f_{\text{TEWL}}$ ), the direct diffusion of water across the epidermis and through the stratum corneum and the evaporation of sensible and insensible sweat ( $f_{se}$ ) released from eccrine and/or apocrine glands<sup>16</sup> (Fig. 2a). Regardless of the source,  $f_w$  is proportional to the difference in water concentration across the epidermis and a reference point in Nilsson's zone, where diffusion dominates over convection<sup>24,25</sup>. This reference point can be set to a location of the valve opening, 6 mm above the skin surface, which lies in the typical Nilsson's zone thickness (between

approximately 6 and 12 mm)<sup>24</sup>. Under the quasi-steady state, Fick's first law applies to  $f_w$ :

$$f_w = \frac{\Delta c}{R} = \frac{c_{sw} - c_{aw}}{R_{sw} + R_{aw}} \quad (2)$$

where  $R$  is the effective diffusive resistance, consisting of contributions from the epidermis ( $R_{sw}$ ) and the air above the skin to the reference level ( $R_{aw}$ ),  $\Delta c$  represents the water vapour concentrations difference between the dermis ( $c_{sw}$ ) and the reference level ( $c_{aw}$ ). The value of  $c_{sw}$  is equivalent to the saturated value at skin temperature ( $T_s$ )<sup>26</sup>. Figure 2b depicts an equivalent resistance circuit model, where  $R_{sw}$  and  $R_{aw}$  act as resistors in series. The contributions of TEWL ( $R_{\text{TEWL}}$ ) and sweat evaporation ( $R_{se}$ ) form  $R_{sw}$  as a parallel connection. Supplementary Note 2 presents empirical validation of the steady state of the chamber microclimate.

As depicted in Fig. 2b (right), the flux path through the open-state EFS chamber differs from that of bare skin. The chamber and valve geometries define the diffusive resistance of this path ( $R_{dw}$ ). This leads to a modified flux expression of equation (3).

$$\tilde{f}_w = \frac{\Delta c}{R_{sw} + R_{dw}} \quad (3)$$

where  $\tilde{f}_w$  is the  $\tilde{f}$  for water vapour. Water vapour diffusion through 6 mm of air with a diffusivity<sup>27</sup> of  $D_w = 24 \text{ mm}^2 \text{s}^{-1}$  yields  $R_{aw} = 250 \text{ s m}^{-1}$ . Rigorous simulations indicate that  $R_{dw}$  consists of two segments,  $R_{dlw}$  and  $R_{d2w}$ , on the basis of the sensor position, such that  $R_{dlw} + R_{d2w} = R_{dw}$ . For this device,  $R_{dlw}$ ,  $R_{d2w}$  and  $R_{dw}$  are 0.6, 5.4 and  $6 \text{ ks m}^{-1}$  and invariant across the practical epidermal and atmospheric conditions (Fig. 2c). The flux density contour in the graph visualizes the occurrence of the  $R_{dw}$ . A higher  $R_{dw}$  than  $R_{aw}$  yields a lower  $\tilde{f}_w$  than  $f_w$ , indicating an occlusion effect. However, the effects of the occlusion on the skin itself are negligible (Supplementary Note 4).

Compensation for the occlusive effect involves the sequential application of equations (2) and (3). First,  $\tilde{f}_w$ ,  $c_{sw}$  and  $R_{d2w}$  yield  $c_{aw}$ , as in equation (4).

$$c_{aw} = c_{sw} + \tilde{f}_w R_{d2w} \quad (4)$$

This result defines  $\Delta c$ , along with  $c_{sw}$ , the value derived from skin-temperature measurements. Substituting  $\Delta c$  and  $\tilde{f}_w$ , along with  $R_{d2w}$ , into equation (3) gives  $R_{sw}$ . Finally, substituting  $R_{sw}$ ,  $\Delta c$  and  $R_{aw}$  yields  $f_w$ , the natural flux density. Supplementary Note 5 details computational and benchtop studies.

Because  $f_w$  is proportional to  $\Delta c$ , which varies according to atmospheric conditions,  $R_{sw}$  better represents the intrinsic skin properties than does  $f_w$ . When the evaporation of sweat is negligible ( $R_{se} = \infty$ ),  $R_{sw}$  measures the skin barrier properties ( $R_{\text{TEWL}}$ ), which are largely determined by the skin barrier at the stratum corneum. Measurements of the electrical impedance of the skin ( $r_s$ ) provide information about the onset of perspiration and, thus, the contribution of  $R_{se}$  to  $R_{sw}$ . Figure 2d illustrates that  $r_s$  determined using a sensor at the underside of the chamber wall identifies three stages of perspiration: absent, insensible and sensible sweating. Collectively, these measurements guide reliable skin barrier assessments across various conditions and scenarios, including multi-day monitoring in hospital or home settings (Fig. 2e,f). Supplementary Note 6 details the perspiration-detection capability.

As a simple example, Fig. 2e shows the recovery of  $R_{sw}$  after the partial removal of the stratum corneum from five healthy adults. The initial  $R_{sw}$  of the forearm decreases from  $25 \text{ ks m}^{-1}$  to about  $7 \text{ ks m}^{-1}$  on average after 30 tape-stripping cycles to remove the stratum corneum. Recovery of  $R_{sw}$  follows a characteristic time of 15.2 days, a period that is similar across participants and consistent with the 14-day stratum corneum turnover timescale<sup>28</sup>. Furthermore, the  $f_w$  value strongly

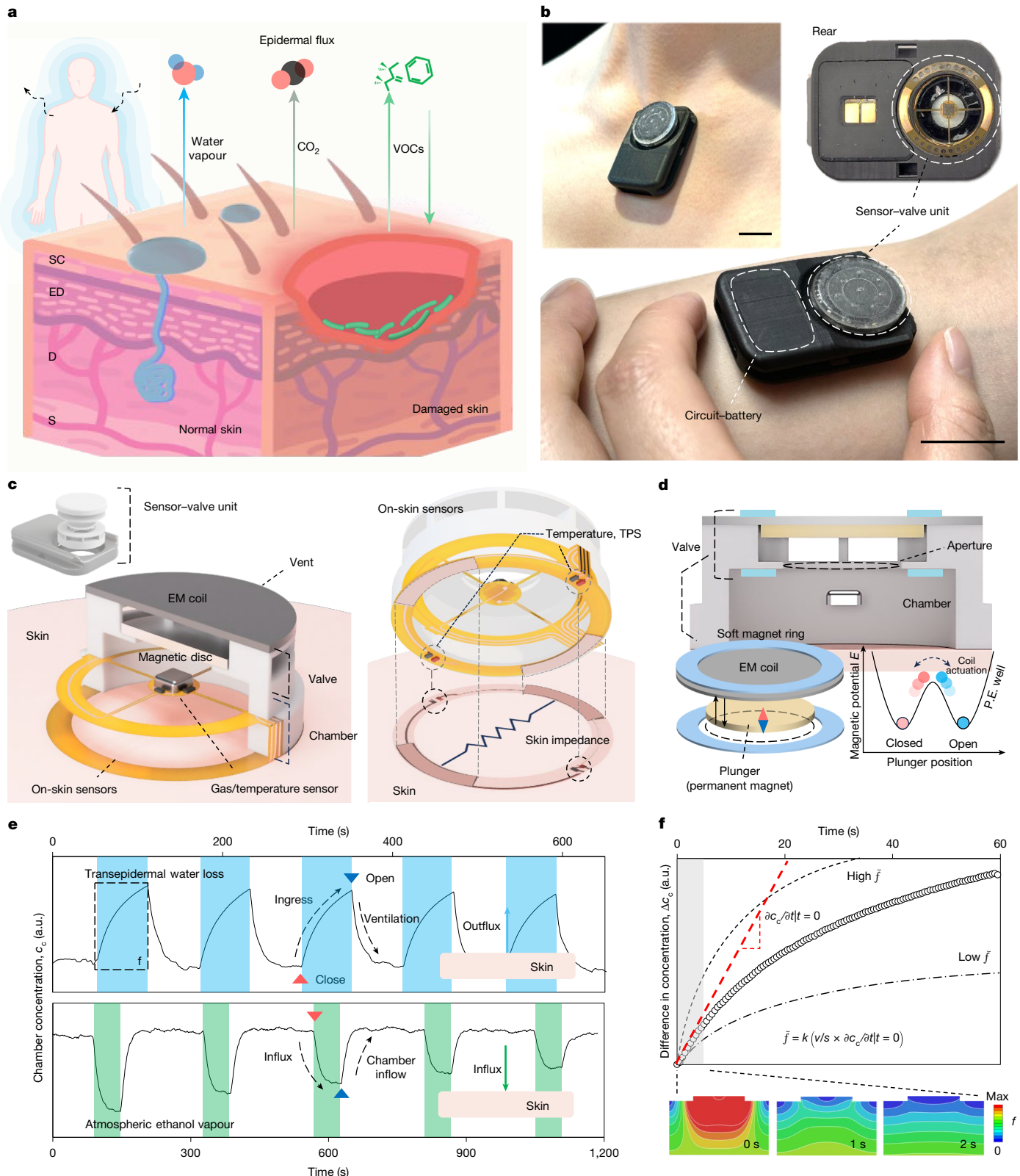


**Fig. 1 | A skin-interfaced system for epidermal flux monitoring.** **a**, Various epidermal fluxes, including water vapour,  $\text{CO}_2$  and VOCs. D, dermis; ED, epidermis; S, subcutaneous tissue. **b**, EFS systems mounted on the skin with major units highlighted: the sensor–valve unit and circuit–battery assembly. Scale bar, 2 cm. **c**, Cross-sectional (left) and bottom (right) view of the sensor–valve unit, featuring the major components: a skin-interfaced chamber with gas and temperature sensors, an electromagnetic (EM) valve and skin-interfaced sensors for temperature, electrical impedance and thermal conductivity. TPS, transient plane source. **d**, Magnetic bistable valve mechanism for

power-efficient actuation. P.E. well, potential energy well. **e**, Time-series data from gas sensors as the valve opens and closes through multiple cycles, showing the effects of the outflux (top; biogenic water vapour) and influx (bottom; atmospheric ethanol vapour). **f**, A single measurement signal. The initial slope of the signal reflects the flux density,  $\bar{f}$ , just before the valve closes to isolate the chamber.  $k$  is the correction coefficient that accounts for the spatiotemporal non-uniformity of concentrations in the microclimate of the isolated chamber. a.u., arbitrary unit.

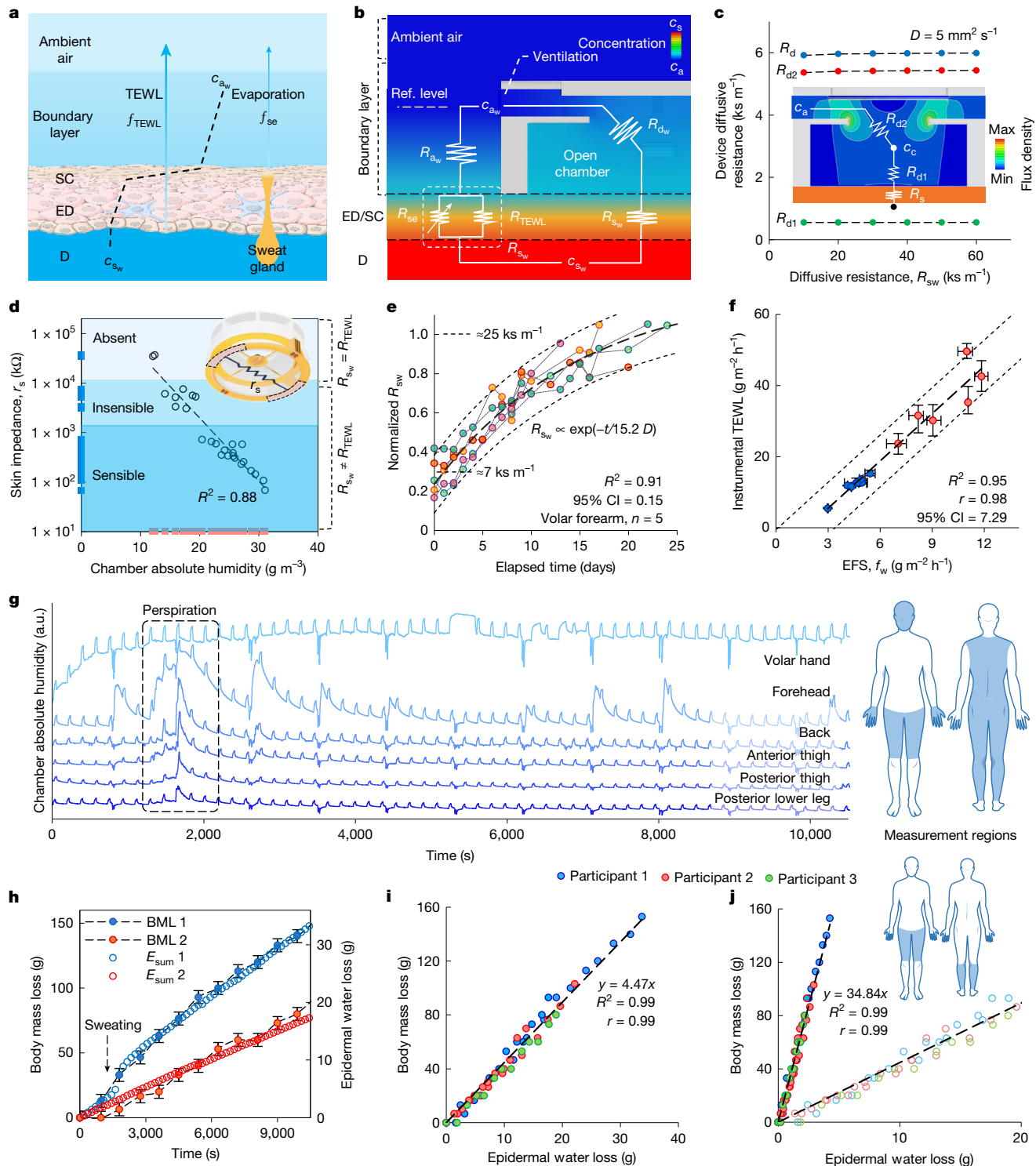


**Fig. 2 | Monitoring of skin barrier properties and fluid loss through measurements of water flux.** **a**, Epidermal water flux ( $f_w$ ) and its contributions from transepidermal water loss ( $f_{TEWL}$ ) and evaporation of sweat ( $f_{se}$ ). **b**, Resistance model of epidermal water transport. The effective diffusive resistances,  $R_{TEWL}$  and  $R_{se}$ , form  $R_{sw}$  as a parallel connection.  $R_{aw}$  and  $R_{dw}$  are constants. **c**, Computational analysis results indicate that  $R_{dw}$  and its constituent segments,  $R_{d1w}$  and  $R_{d2w}$ , are invariant to  $R_{sw}$ . The coloured contour shows flux density. **d**, An exponential decrease in the skin impedance ( $r_s$ ) follows from different levels of perspiration. The skin barrier assessment is valid when there is no perspiration (marked as absent). **e**,  $R_{sw}$  recovery after partial removal of the SC ( $n = 5$  participants). **f**, Comparisons of  $f_w$  to measurements with conventional clinical devices (TEWL, Aquaflux) indicate linear correlations ( $r = 0.98$ ). Data are presented as the mean of three repeated measurements for each apparatus, with

error bars indicating the full range of measurement results. Location, 3 cm below the antecubital fossa. Clinical (psoriasis, atopic dermatitis, ichthyosis and xerosis) and healthy normal conditions are shown in red and blue, respectively ( $n = 14$  participants). **g–j**, The fluid balance was monitored by measuring the water flux. **g**, Time-series data for determining  $f_w$  at six representative skin regions. The periodic positive variations allow for flux measurements. **h**, Agreement between the estimated epidermal water loss ( $E_{sum}$ ) and BML of a human participant for two perspiration settings ( $n = 2$ ). The data in blue were obtained from the recordings in **g**. The error bars indicate the instrumental tolerance of the digital scale ( $\pm 5$  g). **i**, Collective data from five measurements of three participants ( $r = 0.99$ ): 181 cm, 88 kg, male (participant 1); 168 cm, 66 kg, male (participant 2); 157 cm, 51 kg, female (participant 3). **j**, A reduced set of skin regions (anterior thigh and posterior lower leg, filled data points) yields a similar level of correlation ( $r = 0.99$ ).

correlates ( $r = 0.98$ ) with results from a condenser-type instrument used for healthy and impaired skin conditions, including psoriasis, atopic dermatitis, ichthyosis and xerosis (Fig. 2f). Supplementary Note 7 summarizes additional capabilities.

This type of flux assessment also has relevance for monitoring fluid homeostasis. In healthy adults, insensible water loss accounts for about 15% of the total water loss from respiration, perspiration, urination and defecation<sup>29</sup>, with contributions of up to 50% in severe cases in neonates<sup>20</sup>. Continuous measurements of epidermal water flux are therefore important for managing fluid balance<sup>30</sup>. Figure 2g–j summarizes the unique capabilities of the EFS in this context. Simultaneous recordings with devices at six regions of the body capture the  $f_w$  every 3 min ( $\Delta t$ ) for 3 h. For reference, separate measurements quantify body mass loss (BML) every 15 min. Without water intake and excretion, BML represents insensible water loss. The estimated epidermal water loss ( $E_j$ ) as a function of time is calculated by accumulating fluxes ( $f_j^i$ ) weighted by the regional skin area ( $A_j$ ) (equation (5)). The superscript and subscript denote the measurement order and skin region:

$$E_j = \Delta t \sum_i f_j^i A_j \quad (5)$$

Figure 2g displays the absolute humidity values ( $c_{c_w}$ ) in the chamber, offset for visual clarity. Periodic flux measurements associated with valve actuations resemble features in Fig. 1e, with additional transients due to motion artefacts during BML measurements. Baseline elevations, including the one indicated by the dashed rectangle, result from brief perspiration episodes triggered by emotive stimuli, most notably on the forehead, which has the highest sweating rate<sup>31</sup>.

Figure 2h compares the summation of  $E_j$  across all regions ( $E_{\text{sum}}$ ) with BML data from Fig. 2g (blue). The early inflection reflects accelerated water loss from sweating. The data in red represent experiments with reduced sweating. Measurements from three participants reveal strong agreement between  $E_{\text{sum}}$  and BML ( $r = 0.99$ ; Fig. 2i), suggesting a proportionality between epidermal and respiratory water fluxes, consistent with previous studies<sup>32</sup>. Figure 2j demonstrates that measurements at fewer locations (anterior thigh and calf) yield similar results ( $r = 0.99$ ), demonstrating simple and accurate whole-body insensible water-loss assessment. The filled and hollow points represent  $E_{\text{sum}}$  from all and a reduced number of locations, respectively. Supplementary Note 8 provides further details.

## VOCs, CO<sub>2</sub> and exogenous agents

Various VOCs and CO<sub>2</sub> contribute to the skin flux through the skin microbiome<sup>33</sup> and cutaneous respiration<sup>34</sup>, respectively. Likewise, environmental VOCs can flow into the skin<sup>13</sup>. Measuring both inward and outward fluxes yields unique, complementary insights. Figure 3a, for example, illustrates applications in epidermal hygiene and environmental safety enabled by bilateral flux measurements (Fig. 3b).

Inadequate skin hygiene and skin disorders can cause the unregulated proliferation of microorganisms in the genera *Corynebacterium*, *Staphylococcus* and *Propionibacterium*<sup>34</sup>, increasing outward VOC flux ( $f_{\text{VOC}}$ ) from bacterial degradation of biogenic precursors<sup>34</sup>. Daily measurements near the axilla of 11 ethnically diverse adults who limited their washing for 5 days show gradual (57% on day 1 (D1), 218% on D2) and accelerated (691% after perspiration on D3) increases in  $f_{\text{VOC}}$  compared with D0 (Fig. 3c). Washing on D4 reduces  $f_{\text{VOC}}$  to near D0 levels, supporting the idea that precursor secretion and microflora proliferation contribute to  $f_{\text{VOC}}$  (refs. 35,36). Gender-based comparisons show differences consistent with previous studies<sup>37</sup> (Fig. 3d). Supplementary Note 9 details statistical analyses and variations among people from different ethnic and gender groups.

Moreover, the flux of VOCs and the release of CO<sub>2</sub> can attract haematophagous insects<sup>38</sup>. An integrated CO<sub>2</sub> sensor enables precise

measurements of transcutaneous CO<sub>2</sub> flux ( $f_{\text{CO}_2}$ ), as shown in Fig. 3e. Together these channels enable a comprehensive assessment of hygienic status. The  $f_{\text{CO}_2}$  also enables the non-invasive estimation of arterial CO<sub>2</sub>, requiring episodic use of bulky stationary systems at specialized facilities<sup>39</sup>. The long-term continuous  $f_{\text{CO}_2}$  monitoring made possible by wearable systems such as the EFS would be of benefit in various medical contexts, including for determining metabolic anomalies, such as acidosis<sup>39</sup>.

Inward flux measurements serve complementary purposes. The entry of exogenous atmospheric substances ( $f_x$ ) through the skin can pose health hazards<sup>13,40</sup>. The  $x$  and  $i$  denote substance and inward flux, respectively. Figure 3f illustrates the concept of transepidermal chemical diffusive resistance ( $R_{s_x}$ ), a measure of skin barrier function against substances, such as concentrated solvent vapours in industrial settings. Differing from  $R_{s_w}$ ,  $R_{s_x}$  accounts for specific chemical effects on the skin. The compensation scheme described previously applies to yield  $k$ ,  $R_{d_x}$ ,  $\bar{f}_x$ ,  $\Delta c$  and subsequently  $R_{s_x}$  and  $f_x^i$  as in the case of water vapour, with adjustments for material diffusivity and the inverted concentration gradient. For example, ethanol diffusivity in air ( $D_{\text{Ethanol}} = 16 \text{ mm}^2 \text{s}^{-1}$ )<sup>41</sup> yields a  $k = 0.81$ . For xenobiotic solvents,  $c_{s_x}$  can be assumed to be zero<sup>42</sup>. Supplementary Note 5 details this scheme.

One analysis measures the inward flux of concentrated ethanol vapour (about 200 ppm) on the volar forearm, which is of interest because of the potential of ethanol to enhance the penetration of other compounds<sup>43</sup>. The experiments compare bare skin, skin after tape stripping of the stratum corneum and skin with an aluminium foil barrier. In Fig. 3g, the valve closure causes no  $c_{s_{\text{Ethanol}}}$  change for the aluminium-covered skin, whereas the bare skin displays a distinct decrease, indicating that the  $c_{s_{\text{Ethanol}}}$  variation reflects the  $f_{\text{Ethanol}}^i$ . The graphs are offset for clarity. Figure 3h compares  $R_{s_w}$  and  $R_{s_{\text{Ethanol}}}$  across three conditions. Unlike  $R_{s_w}$ , which shows a constant value over consecutive measurements,  $R_{s_{\text{Ethanol}}}$  increases and converges to certain levels after about 20 min of exposure. The  $R_{s_{\text{Ethanol}}}$  values in Fig. 3h correspond to these saturation values. For bare skin, the saturation  $R_{s_{\text{Ethanol}}}$  is about one-third of  $R_{s_w}$ , consistent with reports of higher ethanol permeabilities in the skin<sup>44</sup>. Skin with partially removed stratum corneum has a higher  $R_{s_{\text{Ethanol}}}$ . This could result from ethanol dissolving into, rather than permeating, the stratum corneum, which is lipid-rich, ethanol-soluble membrane<sup>44</sup>. This same mechanism could also explain the  $R_{s_{\text{Ethanol}}}$  saturation.

Radiative forms of energy, such as ultraviolet (UV) light exposure, pose a different kind of environmental hazard to the skin that can also be quantified through skin flux. Figure 3i shows that  $f_{\text{VOC}}$  increases with UV dosage. Cellular analysis of the oxidative tissue damage after UV irradiation captures 8-OHdG, a biomarker for oxidized DNA (Fig. 3j), suggesting that reactive oxygen species are generated in the irradiated skin. Reactive oxygen species can degrade cellular and intra-cellular biomolecules, producing volatile by-products that could contribute to detectable VOCs<sup>45,46</sup>. These results demonstrate that  $f_{\text{VOC}}$  measurement enables the analysis of UV-induced oxidative stress in skin tissues. An exploratory investigation of the chemical composition of UV-induced skin VOCs identifies more than ten chemical species that are probably involved in complex photochemical pathways. The Methods section and Supplementary Note 10 provide the experimental and analytic details.

## Comprehensive wound monitoring

As with UV-induced skin damage, wounds create an outward flux owing to altered skin barrier function and pathogenic processes<sup>47</sup>. These fluxes provide insights into wound status (Fig. 4a). Experiments with models of healthy mice and mice with type 2 diabetes during re-epithelialization capture different flux behaviours. Figure 4b shows the time evolution of chamber concentrations of water and VOCs from an excisional dermal wound on the back of a healthy mouse. Although

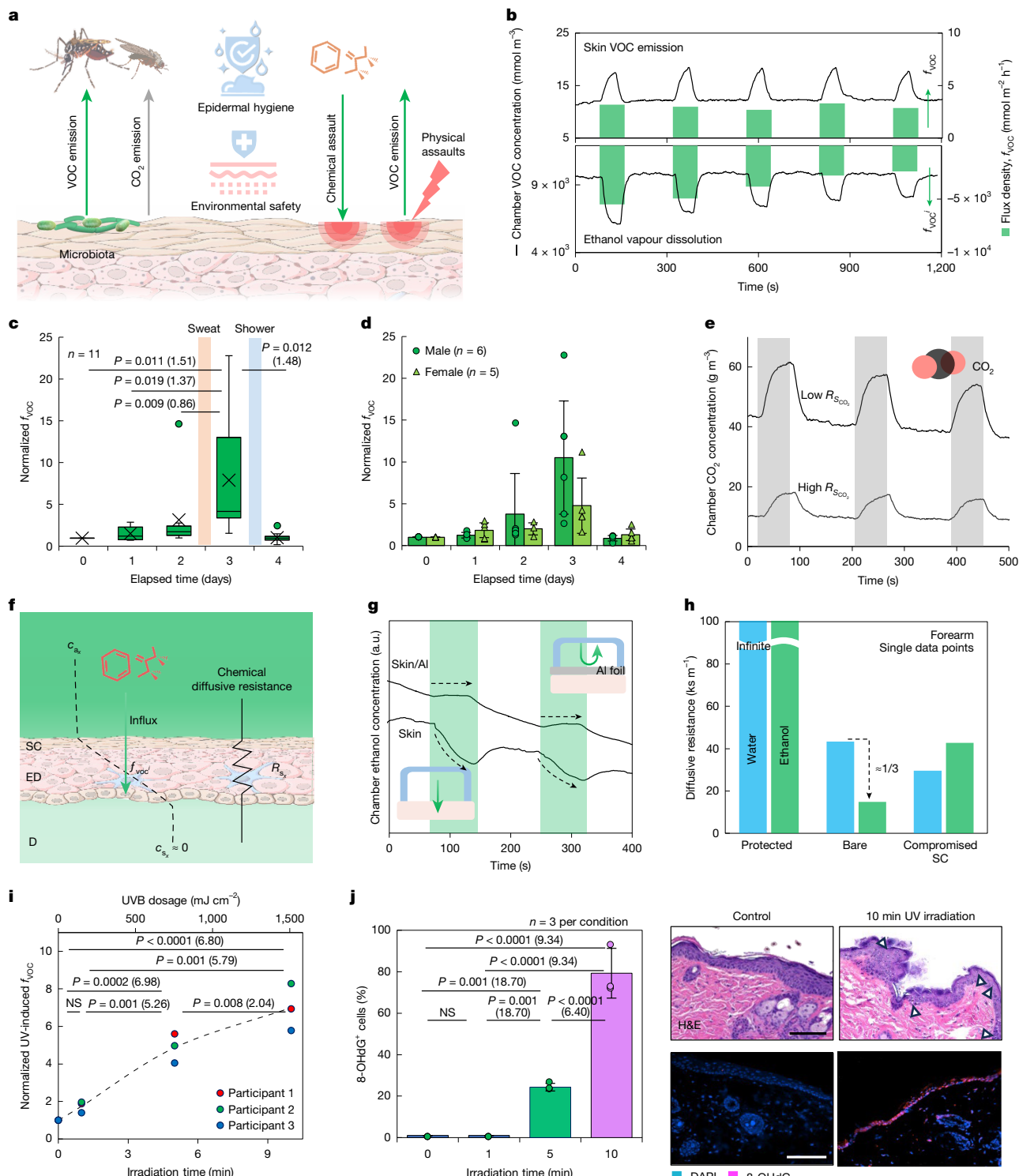


**Fig. 3 | Epidermal flux of VOCs, CO<sub>2</sub> and exogenous agents.** **a**, Modes of VOC and CO<sub>2</sub> fluxes at the skin, associated with epidermal hygiene status and environmental safety. **b**, Example of outward (top) and inward (bottom) epidermal VOC fluxes. **c,d**, Epidermal flux for hygiene assessment. **c**, Changes in epidermal VOC flux density by skin hygienic status. Data are the minimum, maximum, first and third quartiles, mean (X), median (horizontal bar) and outliers (circles) (n = 11 participants). **d**, Comparison between male (n = 6) and female (n = 5) participants. Data are mean ± s.d. **e**, Time-series data associated with the outward flux of CO<sub>2</sub>, corresponding to higher and lower diffusive resistances. **f–h**, Epidermal flux and environmental skin assaults. **f**, Concept of transepidermal chemical diffusive resistance. **g**, Changes in the ethanol-vapour concentration in the chamber microclimate for cases with and without an aluminium barrier. **h**, Comparison of the diffusive resistances of water ( $R_{s_w}$ )

and ethanol ( $R_{s_{Ethanol}}$ ) for three skin conditions: with and without aluminium barrier and with compromised SC. **i,j**, Epidermal outward flux of VOCs in response to radiative assaults. **i**, VOC flux increase after UV irradiation of mouse skin (n = 3 mice). **j**, Increasing cellular oxidative stress marker (8-OHdG) activity with increasing irradiation dosage. Left, the 8-OHdG activity in mice (n = 3 biologically independent mice per condition). Data are mean ± s.d. Right, representative, stained dissection images. The arrows indicate the damaged cells. A repeated measures analysis of variance (ANOVA) (d.f. = 10) (c) or one-way ANOVA (d.f. = 2) (i and j) followed by post hoc pairwise comparisons using the least-significant difference method with 95% confidence intervals were used for analysis. The P values and effect sizes (Cohen's  $d$ , parentheses) are shown in the graphs. Scale bar, 100 μm.

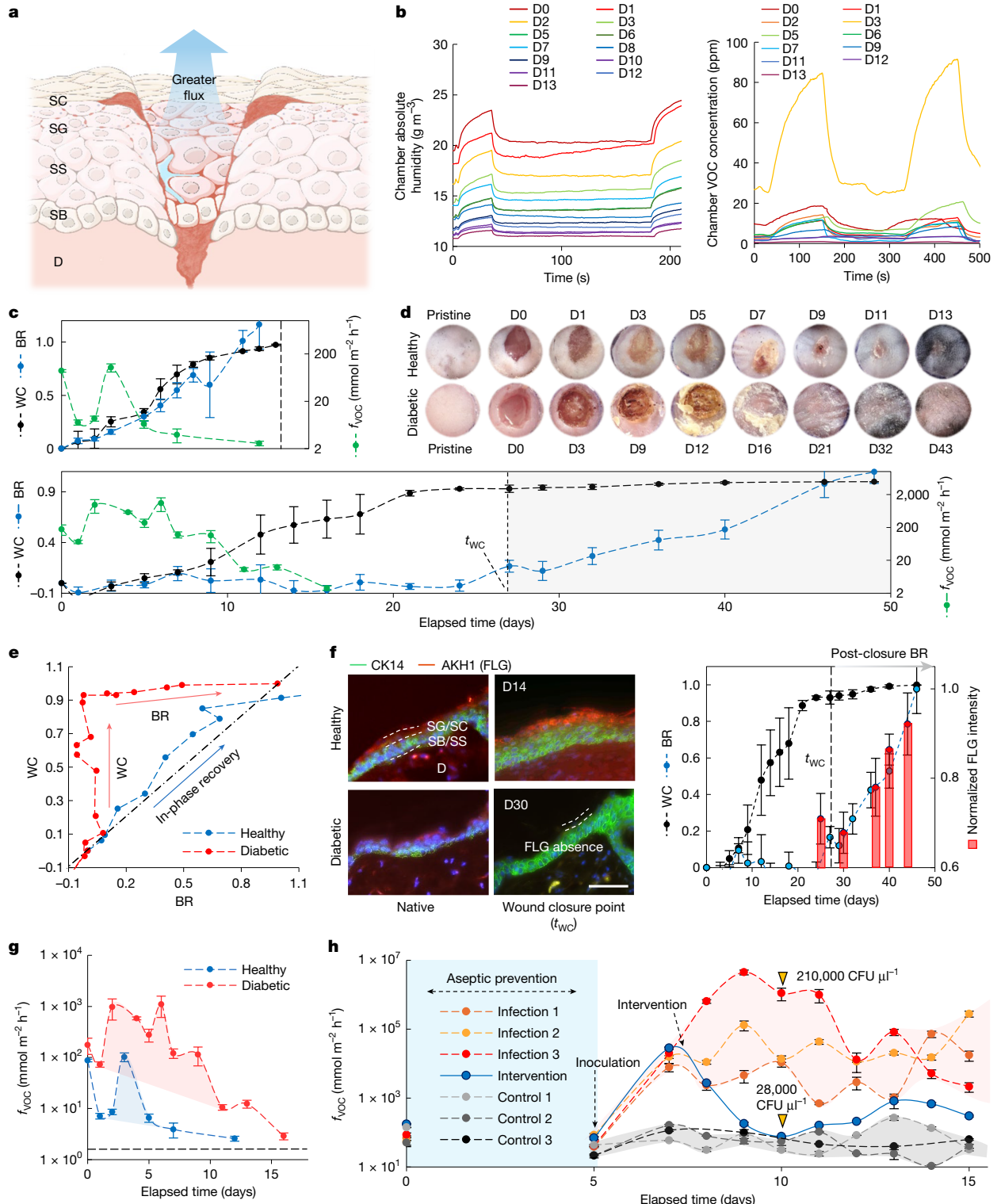


**Fig. 4 | Monitoring of outward VOC and water flux for applications in wound healing.** **a**, Compromised skin barriers in wounds result in elevated outward and inward epidermal fluxes. SB, stratum basale; SS, stratum spinosum. **b**, Transitions of water vapour (left) and VOC (right) flux values throughout the wound-healing process in healthy mice. **c**, Normalized recovery parameters and VOC flux changes for healthy ( $n = 7$ ) and type 2 diabetic ( $n = 7$ ) mice. The time axis is shared. The vertical dashed lines mark the completion of healing. Data are mean  $\pm$  s.e.m. BR, barrier restoration; WC, wound closure. **d**, Visual transition of the wound sites. Image diameter, 10 mm. **e**, Comparison wound-healing pathways in healthy and diabetic mice by water vapour flux ( $f_w$ ) analysis. **f**, Immunofluorescence analysis of delayed keratinocyte terminal differentiation in the diabetic group. Left, representative stained dissection

images of the wound tissues obtained from biologically independent samples of healthy ( $n = 12$ ,  $n = 6$  per condition) and diabetic ( $n = 16$ ,  $n = 8$  per condition) mice. Green, CK14; red, FLG. Scale bar, 50  $\mu\text{m}$ . Right, post-closure FLG activity increase compared with wound closure and barrier restoration changes. The barrier restoration and wound closure are derived from the bottom section of **c**. The FLG intensity was analysed using 48 ( $n = 8$  per condition) diabetic samples. Data are mean  $\pm$  s.e.m. **g**, Early increases in the VOC flux ( $f_{\text{VOC}}$ ) indicate the healthy and anomalous inflammatory phases of the healthy ( $n = 6$ ) and diabetic ( $n = 6$ ) mice. The dashed line is the native level. Data are mean  $\pm$  s.e.m. **h**, Wound infection monitoring capability. Onset and exponential increase in VOC emission from infected wounds in mice ( $n = 7$  mice). The blue line shows the efficacy of the disinfection intervention. Data are mean  $\pm$  s.d. from three measurements.

# Article

$f_w$  gradually decreases to a baseline level characterized by healthy skin,  $f_{VOC}$  temporarily increases during the early stages of recovery before gradually returning to the baseline. These fluxes thus convey correlated yet independent information.

Figure 4c summarizes the healing processes of these two groups through  $f_{VOC}$ , barrier restoration and wound closure. The latter two normalized parameters ( $\tilde{p}$ ) are calculated by equation (6):

$$\tilde{p} = \frac{p - p_0}{p_n - p_0} \quad (6)$$

where  $p$  is  $R_{sw}$  for barrier restoration and wound area for wound closure, with  $n$  and  $0$  denoting healthy skin and pristine wound, respectively. On average, wound closure takes 13 and 27 days for the healthy and diabetic groups, respectively, consistent with previous reports<sup>48</sup> (Fig. 4d).

Figure 4e summarizes qualitative differences in the two wound-healing pathways captured by  $f_w$ . By this metric, skin barrier function with healthy mice tracks the wound closure process. By contrast, the diabetic group fails to recover the barrier function by the wound closure point ( $t_{wc}$ ), with post-closure barrier restoration over the next 3 weeks. Figure 4f suggests a link of this delayed restoration with impaired keratinocyte differentiation associated with hyperglycaemic conditions<sup>49</sup>. Filaggrin (FLG) is a hallmark of the matured stratum granulosum<sup>50</sup>, where the tight junctions form the secondary skin barrier mechanism<sup>51</sup>. Mice in the diabetic group after  $t_{wc}$  (D30) lack FLG activity, whereas the haematoxylin and eosin (H&E) staining results support formation of the stratum granulosum, suggesting the presence of immature stratum granulosum that is unable to restore healthy skin barrier function. As shown in Fig. 4f, FLG activity restores along the post-closure barrier restoration period, aligning with the  $f_w$  data. These findings demonstrate that flux measurements can reveal physiological anomalies in a non-contact manner without disrupting the wound bed or interfering with the healing process. Supplementary Note 11 offers additional analysis.

Inflammation, an essential stage in healing, can lead to the production of various molecular markers, some of which contribute to VOC flux<sup>11,22,52</sup>. The transient increase in this parameter early in the healing process in healthy mice aligns with the expected timing of the inflammatory response<sup>53</sup>. By contrast, measurements suggest anomalous behaviour of the increase in VOC flux in diabetic mice, aligning with a dysregulated inflammatory response (Fig. 4g). Bacterial growth and biofilm formation at infected wounds can also contribute to the release of VOCs<sup>11,23,54</sup>, as demonstrated in a study using mice with infected wounds. Results indicate that whereas the  $f_{VOC}$  values of the control group remain low, the infection group shows an approximately 100-fold increase 2 days after the introduction of bacteria (Fig. 4h). Antibacterial treatment reduces  $f_{VOC}$  close to control levels and significantly lowers bacterial burden (28,000 colony forming units (CFU)  $\mu\text{l}^{-1}$ ) compared with untreated infected wounds (210,000 CFU  $\mu\text{l}^{-1}$ ). The Methods section and Supplementary Note 12 cover further details, including the study of an ex vivo porcine wound model. Collectively, these results indicate that unsupervised EFS users can assess wound-healing status, such as tissue integrity, wound closure and bacterial infection, by tracking the  $f_w$  and  $f_{VOC}$  evolutions and identifying an abrupt exponential increase in  $f_{VOC}$ .

## Outlook

The technology introduced here has broad implications in clinical care, and particularly for vulnerable populations, such as infants, patients and older people with immature, damaged or diminished skin barriers. (Supplementary Note 13). These and other individuals could also benefit from data to guide triage, treatment and monitoring of chemical or radiative burns or ozone-associated skin damage. Further

engineering improvements, including dressing-embedded form factors, could enhance clinical use by enabling conformal yet conservative skin coupling (Supplementary Notes 14 and 15). Measurements of VOC and  $\text{CO}_2$  fluxes could also benefit the general population by enabling disease control and monitoring of exposure to hazardous environmental agents other than ethanol. As outlined in Supplementary Note 16, future developments could enable the production of EFSs with high chemical selectivity for detailed wound-healing diagnostics or the early detection of various diseases affecting internal organs.

## Online content

Any methods, additional references, Nature Portfolio reporting summaries, source data, extended data, supplementary information, acknowledgements, peer review information; details of author contributions and competing interests; and statements of data and code availability are available at <https://doi.org/10.1038/s41586-025-08825-2>.

1. Sun, L. et al. All-solution-processed ultraflexible wearable sensor enabled with universal trilayer structure for organic optoelectronic devices. *Sci. Adv.* **10**, eadk9460 (2024).
2. Chung, H. U. et al. Skin-interfaced biosensors for advanced wireless physiological monitoring in neonatal and pediatric intensive-care units. *Nat. Med.* **26**, 418–429 (2020).
3. Koh, A. et al. A soft, wearable microfluidic device for the capture, storage, and colorimetric sensing of sweat. *Sci. Transl. Med.* **8**, 366ra165 (2016).
4. Nyein, H. Y. Y. et al. A wearable microfluidic sensing patch for dynamic sweat secretion analysis. *ACS Sens.* **3**, 944–952 (2018).
5. Shin, J. et al. Wireless, soft sensors of skin hydration with designs optimized for rapid, accurate diagnostics of dermatological health. *Adv. Healthc. Mater.* **12**, e2202021 (2023).
6. Lee, J., Kim, D., Sul, H. & Ko, S. H. Thermo-haptic materials and devices for wearable virtual and augmented reality. *Adv. Funct. Mater.* **31**, 2007376 (2021).
7. Yu, X. et al. Skin-integrated wireless haptic interfaces for virtual and augmented reality. *Nature* **575**, 473–479 (2019).
8. Kang, B. B., Choi, H., Lee, H. & Cho, K.-J. Exo-glove poly II: a polymer-based soft wearable robot for the hand with a tendon-driven actuation system. *Soft Robot.* **6**, 214–227 (2019).
9. Fluhr, J. W., Feingold, K. R. & Elias, P. M. Transepidermal water loss reflects permeability barrier status: validation in human and rodent *in vivo* and *ex vivo* models. *Exp. Dermatol.* **15**, 483–492 (2006).
10. Berenguer, C. V., Pereira, F., Pereira, J. A. M. & Camara, J. S. Volatilomics: an emerging and promising avenue for the detection of potential prostate cancer biomarkers. *Cancers* **14**, 3982 (2022).
11. Shirasu, M. & Touhara, K. The scent of disease: volatile organic compounds of the human body related to disease and disorder. *J. Biochem.* **150**, 257–266 (2011).
12. Peabody, J. L., Willis, M. M., Gregory, G. A., Tooley, W. H. & Lucey, J. F. Clinical limitations and advantages of transcutaneous oxygen electrodes. *Acta Anaesthesiol. Scand.* **68**, 76–82 (1978).
13. Aravaiskaia, E. et al. The impact of airborne pollution on skin. *J. Eur. Acad. Dermatol. Venereol.* **33**, 1496–1505 (2019).
14. Zhong, B., Jiang, K., Wang, L. & Shen, G. Wearable sweat loss measuring devices: from the role of sweat loss to advanced mechanisms and designs. *Adv. Sci.* **9**, e2103257 (2022).
15. Baker, L. B. Sweating rate and sweat sodium concentration in athletes: a review of methodology and intra/interindividual variability. *Sports Med.* **47**, 111–128 (2017).
16. Alexander, H., Brown, S., Danby, S. & Flohr, C. Research techniques made simple: transepidermal water loss measurement as a research tool. *J. Invest. Dermatol.* **138**, 2295–2300 (2018).
17. Tagami, H., Kobayashi, H. & Kikuchi, K. A portable device using a closed chamber system for measuring transepidermal water loss: comparison with the conventional method. *Skin Res. Technol.* **8**, 7–12 (2002).
18. Klotz, T., Ibrahim, A., Maddern, G., Capplash, Y. & Wagstaff, M. Devices measuring transepidermal water loss: a systematic review of measurement properties. *Skin Res. Technol.* **28**, 497–539 (2022).
19. Imhof, R. E. et al. New instrument for measuring water vapor flux density from arbitrary surfaces. *IFSCC Mag.* **5**, 297–301 (2002).
20. Sung, S. I. et al. Insensible water loss during the first week of life of extremely low birth weight infants less than 25 gestational weeks under high humidification. *Neonatal Med.* **20**, 51–57 (2013).
21. Cramer, M. N., Gagnon, D., Laitano, O. & Crandall, C. G. Human temperature regulation under heat stress in health, disease, and injury. *Physiol. Rev.* **102**, 1907–1989 (2022).
22. Sethi, S., Nanda, R. & Chakraborty, T. Clinical application of volatile organic compound analysis for detecting infectious diseases. *Clin. Microbiol. Rev.* **26**, 462–475 (2013).
23. Thomas, A. N. et al. Novel noninvasive identification of biomarkers by analytical profiling of chronic wounds using volatile organic compounds. *Wound Repair Reg.* **18**, 391–400 (2010).
24. Nilsson, G. E. Measurement of water exchange through skin. *Med. Biol. Eng. Comput.* **15**, 209–218 (1977).
25. Meyer, A. *Evaporation from Lakes and Reservoirs: A Study Based on Fifty Years' Weather Bureau Records* (Minnesota Resources Commission, 1942).
26. Stockdale, M. Water diffusion coefficients versus water activity in stratum corneum: a correlation and its implications. *J. Soc. Cosmet. Chem.* **29**, 625–639 (1978).
27. Merlivat, L. Molecular diffusivities of  $\text{H}_2^{16}\text{O}$ ,  $\text{HD}^{16}\text{O}$ , and  $\text{H}_2^{18}\text{O}$  in gases. *J. Chem. Phys.* **69**, 2864–2871 (1978).

28. Jansen, L. H., Hojyo-Tomoko, M. T. & Kligman, A. M. Improved fluorescence staining technique for estimating turnover of the human stratum corneum. *Br. J. Dermatol.* **90**, 9–12 (1974).
29. Scales, K. & Pilsworth, J. The importance of fluid balance in clinical practice. *Nurs. Stand.* **22**, 50 (2008).
30. Perren, A., Markmann, M., Merlani, G., Marone, C. & Merlani, P. Fluid balance in critically ill patients. Should we really rely on it? *Minerva Anestesiol.* **77**, 802–811 (2011).
31. Taylor, N. A. S. & Machado-Moreira, C. A. Regional variations in transepidermal water loss, eccrine sweat gland density, sweat secretion rates and electrolyte composition in resting and exercising humans. *Extrem. Physiol. Med.* **2**, 4 (2013).
32. Yamada, Y. et al. Variation in human water turnover associated with environmental and lifestyle factors. *Science* **378**, 909–915 (2022).
33. Fitzgerald, L. R. Cutaneous respiration in man. *Physiol. Rev.* **37**, 325–336 (1957).
34. Troccaz, M. et al. Mapping axillary microbiota responsible for body odours using a culture-independent approach. *Microbiome* **3**, 3 (2015).
35. Martin, A. et al. A functional ABCC11 allele is essential in the biochemical formation of human axillary odor. *J. Invest. Dermatol.* **130**, 529–540 (2010).
36. Leyden, J. J. et al. The microbiology of the human axilla and its relationship to axillary odor. *J. Invest. Dermatol.* **77**, 413–416 (1981).
37. Baker, L. B. Physiology of sweat gland function: the roles of sweating and sweat composition in human health. *Temperature* **6**, 211–259 (2019).
38. Barrozo, R. B. & Lazzari, C. R. The Response of the blood-sucking bug *Triatomina infestans* to carbon dioxide and other host odours. *Chem. Senses* **29**, 319–329 (2004).
39. Eberhard, P. The design, use, and results of transcutaneous carbon dioxide analysis: current and future directions. *Anesth. Analg.* **105**, S48–S52 (2007).
40. Huss-Marp, J. et al. Influence of short-term exposure to airborne Der p 1 and volatile organic compounds on skin barrier function and dermal blood flow in patients with atopic eczema and healthy individuals. *Clin. Exp. Allergy* **36**, 338–345 (2006).
41. Lapuerta, M., Hernández, J. P. & Agudelo, J. R. An equation for the estimation of alcohol-air diffusion coefficients for modelling evaporation losses in fuel systems. *Appl. Therm. Eng.* **73**, 539–548 (2014).
42. Weschler, C. J. & Nazaroff, W. W. Dermal uptake of organic vapors commonly found in indoor air. *Environ. Sci. Technol.* **48**, 1230–1237 (2014).
43. Berner, B. et al. Ethanol: water mutually enhanced transdermal therapeutic system II: skin permeation of ethanol and nitroglycerin. *J. Pharm. Sci.* **78**, 402–407 (1989).
44. Lachenmeier, D. W. Safety evaluation of topical applications of ethanol on the skin and inside the oral cavity. *J. Occup. Med. Toxicol.* **3**, 26 (2008).
45. Morliere, P., Moysan, A. & Tirache, I. Action spectrum for UV-induced lipid peroxidation in cultured human skin fibroblasts. *Free Radic. Biol. Med.* **19**, 365–371 (1995).
46. Kochevar, I. E. UV-induced protein alterations and lipid oxidation in erythrocyte membranes. *Photochim. Photobiol.* **52**, 795–800 (1990).
47. Morgado, P. I., Aguiar-Ricardo, A. & Correia, I. J. Asymmetric membranes as ideal wound dressings: an overview on production methods, structure, properties and performance relationship. *J. Memb. Sci.* **490**, 139–151 (2015).
48. Galiano, R. D., Michaels, J. V., Dobryansky, M., Levine, J. P. & Gurtner, G. C. Quantitative and reproducible murine model of excisional wound healing. *Wound Rep. Reg.* **12**, 485–492 (2004).
49. Hu, S. C.-S. & Lan, C.-C. E. High-glucose environment disturbs the physiologic functions of keratinocytes: focusing on diabetic wound healing. *J. Dermatol. Sci.* **84**, 121–127 (2016).
50. Sandilands, A., Sutherland, C., Irvine, A. D. & McLean, W. H. I. Filaggrin in the frontline: role in skin barrier function and disease. *J. Cell Sci.* **122**, 1285–1294 (2009).
51. Furuse, M. et al. Claudin-based tight junctions are crucial for the mammalian epidermal barrier: a lesson from claudin-1-deficient mice. *J. Cell Biol.* **156**, 1099–1111 (2002).
52. Duffy, E. & Morrin, A. Endogenous and microbial volatile organic compounds in cutaneous health and disease. *Trends Anal. Chem.* **111**, 163–172 (2019).
53. Reinke, J. M. & Sorg, H. Wound repair and regeneration. *Eur. Surg. Res.* **49**, 35–43 (2012).
54. Ashrafi, M. et al. Volatile organic compound detection as a potential means of diagnosing cutaneous wound infections. *Wound Repair Regen.* **25**, 574–590 (2017).

**Publisher's note** Springer Nature remains neutral with regard to jurisdictional claims in published maps and institutional affiliations.

Springer Nature or its licensor (e.g. a society or other partner) holds exclusive rights to this article under a publishing agreement with the author(s) or other rightsholder(s); author self-archiving of the accepted manuscript version of this article is solely governed by the terms of such publishing agreement and applicable law.

© The Author(s), under exclusive licence to Springer Nature Limited 2025

# Article

## Methods

### Device fabrication

**Soft magnet.** Magnetite nanoparticles (50–100 nm, Merck) mixed and dispersed thoroughly in a prepolymer to polydimethylsiloxane (PDMS; Sylgard 184, Dow; 10:1 mixing ratio) at 20 wt% served as the base material for the soft magnet component of the programmable, bistable valve assembly. Degassing the mixture, spin-coating it on a Petri dish for 30 s at 400 rpm and then thermally curing at 50 °C for 12 h completed the process. A laser cutting process defined the required annulus shapes (inner diameter, 8.4 mm; outer diameter, 14.2 mm) for integration into the valve.

**Circuit.** A flexible printed circuit board with a planar electromagnetic coil formed the platform for mounting a Li-polymer battery (130 mAh) and various commercial electronic components, including sensors for water vapour (BME280, Bosch) VOCs (BME680, Bosch) and CO<sub>2</sub> (STC31-R3, Sensirion). Supplementary Note 1 presents details on the circuit architecture.

**Device assembly.** A 3D printing process (Form 3+, Formlabs) defined the frame of the system to house the circuit–battery assembly and the soft magnet structures and magnetic plunger. A mechanical locking mechanism joined the top and bottom frames to complete the enclosure.

### Data acquisition and analysis

A secured data-management server mediated the upload, archiving and downloading of raw measurement data from EFS devices connected to the server by a custom smartphone application. Custom Python (v.3.11.0) and Microsoft Visual Basic for Application (v.7.1) codes implementing the analysis principles were used subsequently to process the downloaded raw data in the form of Jason files to derive the measurement results. Supplementary Note 2 covers the analysis principles in detail.

### Benchtop studies

Uncured PDMS resin was used to bond PDMS membranes with various thicknesses to the lids of a small container with a circular opening at the centre. Liquid water or gaseous substances filled the container for different experimental settings. We measured the temperature at the centre of the PDMS membrane and transmembrane permeation in the form of gaseous fluxes. To measure the influx, we used a device that interfaced with the side of the membrane facing the interior of the container. Supplementary Notes 8, 14 and 16 provide information on experimental details.

### Human participant studies

**Inclusion and ethics.** All individuals participated voluntarily and informed consent was obtained before the experiments. The selection of participants was based solely on their suitability for research objectives. Research protocols were approved by the Institutional Review Board at Northwestern University (STU00220121-MOD0002).

**Acclimatization protocol.** Before the device was attached, each participant remained quiet in a resting state for 15 min in an ambient laboratory atmosphere. Data acquisition began 15 min after the device was mounted, again with the participant in a resting state.

**Device comparison.** For experiments in Fig. 2f, Aquaflux (Biox Systems) and EFS were used to examine the same skin area three times each. Each measurement session consisted of an acclimatization period followed by three consecutive measurements at 5-min intervals. For Aquaflux, the participant waited for the same 5-min period in a resting position. The study involved alternating the session

order for each participant to eliminate the potential effects of session order.

**Ethanol influx test.** The participant placed the forearm wearing the EFS in an acrylic box and underwent an acclimatization protocol. Rubber clay sealed the arm opening. Ethanol vapour filled the container through the inlet of the container, and the EFS started the measurements after the injection ended. During the measurement period, a separate VOC sensor monitored the vapour concentration inside the container to control the concentration below the recommended exposure limit<sup>55</sup> of 1,000 ppm.

### Animal studies

**Study design.** Sample size was not predetermined. The number of experiments was determined on the basis of the maximum available resources. The adequacy of the sample size was justified through statistical analyses. Randomization and blinding were not used in this study.

**Animals.** Diabetic (BKS.Cg-m +/+ *Lepr*<sup>db</sup>, 000642; homozygous for *Lepr*<sup>db</sup>) and healthy (C57/BL6) mice aged 8–12 weeks were obtained from Jackson Laboratory. The sex of the mice was assigned as male by the vendor.

**Ethics.** The Institutional Animal Care and Use Committee (IACUC) at Northwestern University approved the in vivo animal studies under protocols IS00018748 and IS00000373, and animal studies were conducted in compliance with these protocols. The housing conditions complied with IACUC standards, maintaining a 14-h light and 10-h dark cycle, ambient temperatures of 18–23 °C (approximately 65–75 °F) and humidity levels between 40 and 60%.

**UV irradiation.** The UV-induced VOC test involved exposing the skin of mice to UV irradiation ( $\lambda_{\text{peak}} = 302 \text{ nm}$ ), emulating sunburn caused by atmospheric UV exposure, which is primarily caused by UV-B<sup>56</sup>. The distance between the UV source (UVP EL series, Analytik Jena) and the mouse skin calibrated the irradiance to 2.4 mW cm<sup>-2</sup>. Supplementary Note 10 covers a more detailed protocol.

**Mouse wound model.** The wound-creation process began with shaving the fur from the dorsal side of each mouse, after which the dermis was excised using a 6-mm diameter punch biopsy (Acuderm). Subsequently, 6-0 nylon sutures (Ethicon) were used to add a sterilized annulus acrylate splint (inner diameter, 10 mm; outer diameter, 12 mm) around the wound to prevent skin contraction. Laser-cut annulus occlusive dressings (TegaDerm, 3M) were used to protect the splint and outer skin. Fluxes were measured to monitor the wound-healing process. Three blinded observers used ImageJ (v.1.54m) to estimate the percentage of wound closure. The wound beds were infected with a suspension of *Staphylococcus aureus* ( $2.25 \times 10^6 \text{ CFU}$ ), a bacterial species that is the leading cause of wound infections in humans<sup>57</sup>, on D5 of wound creation to maintain an aseptic environment during the acute inflammation phase. The disinfection treatment involved removing dead tissues and contamination at the wound bed using cotton swaps soaked with a commercial wound-cleansing solution (Vashe Wound Solution, Urgo Medical North America). Supplementary Note 12 covers a more detailed protocol.

**Tissue processing and immunofluorescence staining.** Animals were euthanized 8, 14, 25, 30, 37, 40 or 44 days after wound creation or immediately after UV exposure in the wound-healing study and UV-induced skin damage analysis. A 10-mm biopsy punch (Acuderm) was used to excise the regenerated wound tissue. The tissue was fixed with 4% paraformaldehyde and embedded in paraffin. The embedded tissues were sectioned and stained for keratin-14 (1:1,000, Abcam),

FLG (1:50, Santa Cruz Biotechnology) and 8-OHdG (1:100, Abcam) and with H&E. Secondary antibodies conjugated to Alexa Fluor 488 or Alexa Fluor 555 (Invitrogen) were used. Control samples included those stained with the secondary antibody without primary antibody. ImageJ (v.1.54m) was used to quantify the fluorescence intensity.

## Statistics

**Regression fitting.** A generalized reduced-gradient non-linear optimization algorithm was used for regression fitting. We used an inverse exponential, linear, negative exponential model for data in Fig. 2d–f,i,j.

**R<sup>2</sup> and r values.** All regression fitting results presented as R<sup>2</sup> values calculated using the standard R<sup>2</sup> formula. Regression fitting results for the comparison of two matrixes are presented as the Pearson's r values calculated using the direct method<sup>58</sup>.

**Confidence intervals.** Data from five or more participants inferring the trend of a population are presented as confidence intervals with a 95% confidence level, calculated using the Student's t-distribution method<sup>59</sup>.

**ANOVAs.** A repeated measures ANOVA (Fig. 3c) and a one-way ANOVA (Fig. 3i,j) were used to analyse the data, after which post hoc pairwise comparisons using the least-significant difference method were applied. The analyses derived P values under 95% confidence intervals. Effect sizes (Cohen's d) were calculated by dividing the difference between means by the pooled standard deviation<sup>60</sup>.

**Software tools.** SPSS (v.24) and Microsoft Excel (v.16.94) were used for the ANOVA test and the other statistical analyses, respectively.

## Reporting summary

Further information on research design is available in the Nature Portfolio Reporting Summary linked to this article.

## Data availability

Data presented in this study, except for human participant data, are available at Dryad (<https://doi.org/10.5061/dryad.bk3j9kdp7>)<sup>61</sup>. Human participant data including protected health information constitutes a limited dataset defined by HIPPA (Health Insurance Portability and Accountability). Completely de-identified human participant data can be provided upon request with a detailed description of the intended use at large to advance science and health. Requests sent to the corresponding author (J.A.R.) by email will be subject to executing a data

use agreement with Northwestern University, which can take up to one month. Source data are provided with this paper.

## Code availability

Custom analysis codes used in this study are available at Zenodo (<https://doi.org/10.5281/zenodo.14884409>)<sup>62</sup>.

55. Rempel, D. M., Amirtharajah, M. & Descatha, A. *CURRENT Occupational and Environmental Medicine* 5th edn (McGraw Hill, 2014).
56. Moore, C. et al. UVB radiation generates sunburn pain and affects skin by activating epidermal TRPV4 ion channels and triggering endothelin-1 signaling. *Proc. Natl Acad. Sci. USA* **110**, E3225–E3234 (2013).
57. Linz, M. S., Mattappallil, A., Finkel, D. & Parker, D. Clinical impact of *Staphylococcus aureus* skin and soft tissue infections. *Antibiotics* **12**, 557 (2023).
58. Pearson, K. Mathematical contributions to the theory of evolution.—III. Regression, heredity, and panmixia. *Philos. Trans. R. Soc. Lond. A* **187**, 253–318 (1896).
59. Student. The probable error of a mean. *Biometrika* **6**, 1–25 (1908).
60. Draper, N. R. & Smith, H. *Applied Regression Analysis* 3rd edn (Wiley, 1998).
61. Shin, J., Song, J., Cho, S., Rogers, J. A non-contact wearable device for monitoring epidermal molecular flux. *Dryad* <https://doi.org/10.5061/dryad.bk3j9kdp7> (2025).
62. Shin, J., Song, J., Cho, S., Rogers, J. A non-contact wearable device for monitoring epidermal molecular flux. *Zenodo* <https://doi.org/10.5281/zenodo.14884409> (2025).

**Acknowledgements** This work is supported by the Querrey-Simpson Institute for Bioelectronics and the Center for Advanced Regenerative Engineering (CARE) at Northwestern University.

J.S. acknowledges support from the National Research Foundation of Korea grant funded by the Korea government (MSIT) (grant no. RS-2024-00358747) and J.W.S. acknowledges support from the National Institute of Diabetes and Digestive and Kidney Diseases (grant no. R01DK131302). A.T. acknowledges support from T32 grant (grant no. EB031527).

**Author contributions** J.S.: conceptualization, hardware and firmware development, methodology, experiments, characterization, investigation, formal analysis, visualization, data curation and writing; J.W.S.: methodology, experiments, characterization, investigation, formal analysis, writing—review and editing; M.T.F.: conceptualization, hardware and firmware development, characterization, writing—review and editing; S.C.: methodology, experiments, characterization, investigation, formal analysis, writing—review and editing; S.L.: computational analyses, writing—review and editing; A.T. and K.R.P.: experiments, characterization; A.G.H.: hardware development, experiments and characterization; H.W.: methodology; S.J.: experiments, characterization; J.T.: firmware development; M.K.: methodology and characterization; K.N.: hardware development; A.Y.: characterization and resources; Y.H.: hardware development; W.S.: hardware development; J.L. and S.P.: skin VOC analysis; J.-H.K.: animal experiment; A.B.: methodology and resources; J.-K.C.: conceptualization, hardware and firmware development and resources; A.S.P.: characterization, resources, writing—review and editing; Y.H.: project administration, supervision; G.A.A.: funding acquisition, project administration, supervision, writing—review and editing; J.A.R.: funding acquisition, project conceptualization, project administration, supervision, writing—review and editing.

**Competing interests** The authors declare no competing interests.

## Additional information

**Supplementary information** The online version contains supplementary material available at <https://doi.org/10.1038/s41586-025-08825-2>.

**Correspondence and requests for materials** should be addressed to Yonggang Huang, Guillermo A. Ameer or John A. Rogers.

**Peer review information** *Nature* thanks Wei Gao, John Ho, Bozhi Tian and the other, anonymous, reviewer(s) for their contribution to the peer review of this work.

**Reprints and permissions information** is available at <http://www.nature.com/reprints>.

Corresponding author(s): John A. Rogers

Last updated by author(s): Feb 19, 2025

## Reporting Summary

Nature Portfolio wishes to improve the reproducibility of the work that we publish. This form provides structure for consistency and transparency in reporting. For further information on Nature Portfolio policies, see our [Editorial Policies](#) and the [Editorial Policy Checklist](#).

### Statistics

For all statistical analyses, confirm that the following items are present in the figure legend, table legend, main text, or Methods section.

n/a Confirmed

- The exact sample size ( $n$ ) for each experimental group/condition, given as a discrete number and unit of measurement
- A statement on whether measurements were taken from distinct samples or whether the same sample was measured repeatedly
- The statistical test(s) used AND whether they are one- or two-sided  
*Only common tests should be described solely by name; describe more complex techniques in the Methods section.*
- A description of all covariates tested
- A description of any assumptions or corrections, such as tests of normality and adjustment for multiple comparisons
- A full description of the statistical parameters including central tendency (e.g. means) or other basic estimates (e.g. regression coefficient) AND variation (e.g. standard deviation) or associated estimates of uncertainty (e.g. confidence intervals)
- For null hypothesis testing, the test statistic (e.g.  $F$ ,  $t$ ,  $r$ ) with confidence intervals, effect sizes, degrees of freedom and  $P$  value noted  
*Give P values as exact values whenever suitable.*
- For Bayesian analysis, information on the choice of priors and Markov chain Monte Carlo settings
- For hierarchical and complex designs, identification of the appropriate level for tests and full reporting of outcomes
- Estimates of effect sizes (e.g. Cohen's  $d$ , Pearson's  $r$ ), indicating how they were calculated

*Our web collection on [statistics for biologists](#) contains articles on many of the points above.*

### Software and code

Policy information about [availability of computer code](#)

Data collection Data was collected from a customized Bluetooth protocol-based App.

Data analysis The raw data in the form of csv or json files were initially processed using custom Python 3.11.0 and Microsoft Visual Basic for Application 7.1 codes. All data (<https://doi.org/10.5061/dryad.bk3j9kdp7>) and custom analysis code (<https://doi.org/10.5281/zenodo.14884409>) are available in the public repository. Additional software involved in data analysis include ImageJ 1.54m, SPSS 24, and Microsoft Excel 16.94.

For manuscripts utilizing custom algorithms or software that are central to the research but not yet described in published literature, software must be made available to editors and reviewers. We strongly encourage code deposition in a community repository (e.g. GitHub). See the Nature Portfolio [guidelines for submitting code & software](#) for further information.

### Data

Policy information about [availability of data](#)

All manuscripts must include a [data availability statement](#). This statement should provide the following information, where applicable:

- Accession codes, unique identifiers, or web links for publicly available datasets
- A description of any restrictions on data availability
- For clinical datasets or third party data, please ensure that the statement adheres to our [policy](#)

Custom analysis code (<https://doi.org/10.5281/zenodo.14884409>) and data presented in this study (<https://doi.org/10.5061/dryad.bk3j9kdp7>), with the exception of human subject data, are available in the public repository. Human subject data including protected health information constitutes a limited data set defined by

HIPPA (Health Insurance Portability and Accountability). Completely de-identified human subject data can be provided upon request with a detailed description of the intended use at large to advance science and health. Requests sent to the corresponding author (Prof. John A. Rogers) via email ([jrogers@northwestern.edu](mailto:jrogers@northwestern.edu)) will be subject to executing a data use agreement with Northwestern University, which can take one month or less.

## Research involving human participants, their data, or biological material

Policy information about studies with [human participants or human data](#). See also policy information about [sex, gender \(identity/presentation\), and sexual orientation](#) and [race, ethnicity and racism](#).

### Reporting on sex and gender

The selection of participants was based solely on their suitability for research objectives. For stratum corneum restoration testing, we included adults without consideration of their sex or gender for tests. For insensible water loss monitoring and hygiene monitoring, equal number of male and female adults were selected based on significant differences in sex or gender that have been previously reported and are described in relevant sections.

### Reporting on race, ethnicity, or other socially relevant groupings

The selection of participants was based solely on their suitability for research objectives. In the study we included adults without consideration of their race or ethnicity for all tests with the exception of hygiene monitoring, where an equal number of adults from three ethnic groups were selected based on significant differences that have been previously reported and presented in relevant sections.

### Population characteristics

Adults ranging in age from 18 to 70 years participated in this study.

### Recruitment

All subjects were recruited randomly without bias from Northwestern University campus in Evanston or Chicago, IL, USA.

### Ethics oversight

Study protocols were approved by the Northwestern Institutional Review Board (STU0020121-MOD0002).

Note that full information on the approval of the study protocol must also be provided in the manuscript.

## Field-specific reporting

Please select the one below that is the best fit for your research. If you are not sure, read the appropriate sections before making your selection.

Life sciences       Behavioural & social sciences       Ecological, evolutionary & environmental sciences

For a reference copy of the document with all sections, see [nature.com/documents/nr-reporting-summary-flat.pdf](https://nature.com/documents/nr-reporting-summary-flat.pdf)

## Life sciences study design

All studies must disclose on these points even when the disclosure is negative.

### Sample size

Sample size was not pre-determined. The number of experiments was determined based on the maximum available resources. The adequacy of the sample size was justified through statistical analysis, including ANOVA and t-tests. For human subject studies, sample size was 5 stratum corneum restoration, 14 for instrumental comparison, 3 for fluid homeostasis monitoring, and 11 for hygiene monitoring. For animal tests, sample size was 3 for UV-induced VOC monitoring, 7 for normal wound monitoring, 7 for diabetic wound monitoring, and 7 for infected wound monitoring. For immunofluorescence analysis, 12 for UV-induced VOC study, for wound healing studies, 18 for normal and 48 for diabetic.

### Data exclusions

No data was excluded.

### Replication

For all experiments, unless otherwise stated in the manuscript, at least three experiments were either replicated or conducted independently and we confirm that all replication attempts fell within the acceptable error range.

### Randomization

This is not relevant to this study. We conducted a prospective, observational single-arm study to evaluate the performance of our sensors. Thus, randomization was not necessary or appropriate.

### Blinding

No blinding was performed. Blinding was not used in this study because it did not involve experiments where bias was a concern.

## Reporting for specific materials, systems and methods

We require information from authors about some types of materials, experimental systems and methods used in many studies. Here, indicate whether each material, system or method listed is relevant to your study. If you are not sure if a list item applies to your research, read the appropriate section before selecting a response.

## Materials & experimental systems

|                                     |   |
|-------------------------------------|---|
| n/a                                 | Involved in the study   |
| <input type="checkbox"/>            | <input checked="" type="checkbox"/> Antibodies                  |
| <input checked="" type="checkbox"/> | <input type="checkbox"/> Eukaryotic cell lines                  |
| <input checked="" type="checkbox"/> | <input type="checkbox"/> Palaeontology and archaeology          |
| <input type="checkbox"/>            | <input checked="" type="checkbox"/> Animals and other organisms |
| <input checked="" type="checkbox"/> | <input type="checkbox"/> Clinical data                          |
| <input checked="" type="checkbox"/> | <input type="checkbox"/> Dual use research of concern           |
| <input checked="" type="checkbox"/> | <input type="checkbox"/> Plants                                 |

## Methods

|                                     |   |
|-------------------------------------|---|
| n/a                                 | Involved in the study                           |
| <input checked="" type="checkbox"/> | <input type="checkbox"/> ChIP-seq               |
| <input checked="" type="checkbox"/> | <input type="checkbox"/> Flow cytometry         |
| <input checked="" type="checkbox"/> | <input type="checkbox"/> MRI-based neuroimaging |

## Antibodies

### Antibodies used

FLG/Filaggrin antibody (AKH1): sc-66192, Santa Cruz Biotechnology. Anti-Cytokeratin 14 antibody: ab119695, Abcam. 8-OHdG antibody (15A3): ab62623, Abcam.

### Validation

The antibodies were validated by the manufacturers as follows.  
 "Filaggrin Antibody (AKH1): sc-66192 is a mouse monoclonal IgG1 kappa light chain antibody that detects Filaggrin protein of human origin by western blotting (WB), immunofluorescence (IF), and immunohistochemistry with paraffin-embedded sections (IHC). Anti-DNA/RNA Damage antibody: ab62623 is a mouse monoclonal antibody that is used in DNA/RNA Damage IHC and immunofluorescence. All our antibodies undergo standard validation and biophysical testing to ensure specificity and where possible includes testing across various applications using positive and negative cell lines, primary cells, cell treatments, and tissue microarrays. We believe this sets the minimum quality standard for antibody validation."  
 "Rabbit Recombinant Monoclonal Cytokeratin 14 antibody: ab119695 is suitable for IHC-P, ICC/IF, Flow Cyt (Intra), WB, IHC-Fr, mIHC and reacts with Human, Mouse, Rat samples. KO Validated: Knock-out (KO) validation is a robust technique used to confirm antibody specificity by testing the antibody of interest in a cell line or tissue that has been engineered to not express the target protein. They were also validated using primary and secondary controls."

## Animals and other research organisms

Policy information about [studies involving animals](#); [ARRIVE guidelines](#) recommended for reporting animal research, and [Sex and Gender in Research](#)

### Laboratory animals

Diabetic (db/db) (BKS.Cg-m +/ Leprdb) mice aged 8-12 weeks and healthy (C57/BL6J) mice aged 8-12 weeks were obtained from the Jackson Laboratory, USA.

### Wild animals

This study did not involve wild animals.

### Reporting on sex

Sex was not considered in the design of the study. The sex of the mice was assigned as male by the vendor.

### Field-collected samples

The study did not involve samples collected from the field.

### Ethics oversight

The Institutional Animal Care and Use Committee (IACUC) at Northwestern University's Center for Comparative Medicine (CCM) approved all animals and procedures prior to experimentation (IS00018748 and IS00000373).

Note that full information on the approval of the study protocol must also be provided in the manuscript.